ACS APPLIED MATERIALS & INTERFACES

www.acsami.org

Research Article

# Separating Cationic and Anionic Redox Activity in the Lithium-Rich Antiperovskite $(Li_2Fe)SO$

Lennart Singer,* Bowen Dong, Mohamed A. A. Mohamed, Frederik L. Carstens, Silke Hampel, Nico Gräßler, and Rüdiger Klingeler*

Cite This: *ACS Appl. Mater. Interfaces* 2024, 16, 40873−40880

Read Online

ACCESS | Metrics & More | Article Recommendations | Supporting Information

**ABSTRACT:** Lithium-rich antiperovskites promise to be a compelling class of high-capacity cathode materials due to the existence of both cationic and anionic redox activity. Little is however known about the effect of separating the electrochemical cationic process from the anionic process and the associated implications on the electrochemical performance. In this context, we report the electrochemical properties of the illustrative example of three different $(Li_2Fe)SO$ materials with a focus on separating cationic from anionic effects. With the high-voltage anionic process, an astonishing electrochemical capacity of around 400 mAh $g^{-1}$ can initially be reached. Our results however identify the anionic process as the cause of poor cycling stability and demonstrate that the fading reported in previous literature is avoided by restricting to only the cationic processes. Following this path, our $(Li_2Fe)SO$-BM500 shows strongly improved performance as indicated by constant electrochemical cycling over 100 cycles at a capacity of around 175 mAh $g^{-1}$ at 1 C. Our approach also allows us to investigate the electrochemical performance of the bare antiperovskite phase excluding extrinsic activity from initial or cycling-induced impurity phases. Our results underscore that synthesis conditions are a critical determinant of electrochemical performance in lithium-rich antiperovskites, especially with regard to the amount of electrochemical secondary phases, while the particle size has not been found to be a crucial parameter. Overall, separating and understanding the effects of the cationic from the anionic redox activity in lithium-rich antiperovskites provides the route to further improve their performance in electrochemical energy storage.

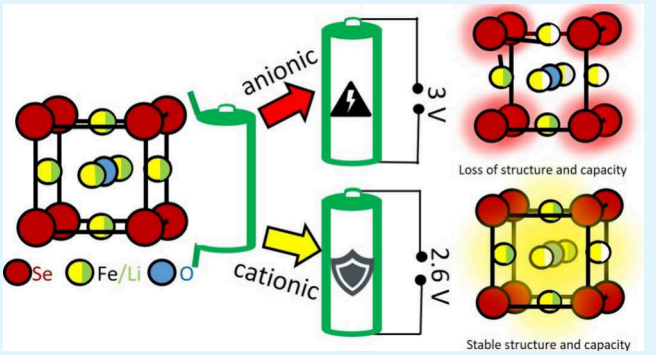


**KEYWORDS:** *Antiperovskites, Cathode, LIB, Anionic redox, Multielectron storage*



## 1. INTRODUCTION

The recent discovery of the lithium-rich antiperovskite compounds characterized by the general formula $(Li_2TM)$-ChO (with TM = Fe, Mn, Co; Ch = S, Se) has significantly broadened the landscape of potential cathode materials for lithium-ion batteries (LIBs).[1] This novel class of materials showcases highly favorable attributes in the context of lithium-ion battery application, including cost effectiveness, utilization of environmentally benign raw materials, efficient lithium diffusion, and the ability of multielectron storage per chemical unit.[2−8] From the so far investigated antiperovskite materials $Li_2FeSO$,[1,4,9−14] $(Li_2Co)SO$,[15] $(Li_2Mn)SO$,[15] $(Li_2Fe_{1-x}Mn_x)$-SO,[9,10,12] $(Li_2Fe_{0.9}Co_{0.1})SO$,[10] $(Li_2Co)SeO$,[15] $(Li_2Mn)SeO$,[15] $(Li_2Fe)S_{1-x}Se_xO$,[16] and $(Li_2Fe)SeO$,[1,14,17] the $(Li_2Fe)SO$ compound captivates with the highest theoretical capacity. Despite the promises of lithium-rich antiperovskites and especially $(Li_2Fe)SO$, their great potential could not be fully exploited due to poor cycling stability (only 66% capacity retention in $(Li_2Fe)SO$ at 0.1 C after 50 cycles).[3]

In our recent works on $(Li_2Fe)SeO$, we have demonstrated the stabilizing effect of selenium as an anion in the antiperovskite structure for the electrochemical performance.[17] We have also shown that the poor cycling stability in this system originates from the high-voltage electrochemical processes causing decomposition of the antiperovskite structure.[14] When cutting off the decomposition reaction, the cycle stability is significantly improved (over 80% capacity retention after 100 cycles for $(Li_2Fe)SeO$ at 1 C in the voltage range from 1 to 2.5 V).[14] A big challenge to further improve the cycling stability in $(Li_2Fe)SeO$ is however the clear separation of the second step of the cationic two-stage iron oxidation reaction from the highly overlapping anionic

Received: April 9, 2024
Revised: July 12, 2024
Accepted: July 15, 2024
Published: July 30, 2024

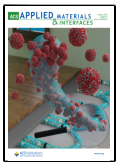




https://doi.org/10.1021/acsami.4c05800
*ACS Appl. Mater. Interfaces* 2024, 16, 40873−40880

decomposition reaction. Studies conducted on the $(Li_2Fe)$-$S_{1-x}Se_xO$ series have unveiled a noteworthy phenomenon to solve this issue: An increase in sulfur content (from $x = 0.1$ to 0.9) correlates with a discernible upward shift in the voltage range corresponding to the anionic oxidation reaction, while the cationic iron reaction remains essentially invariant.[16] This empirical observation offers a route to disentangle and hence separately investigate the cationic and suggested anionic reactions by studying the S-end member of the doping series which manifests the most distinct voltage difference between the cationic and the anionic reactions.

Building on these results, we present the electrochemical properties of three differently mechanochemically synthesized $(Li_2Fe)SO$ samples and explore the effect of separating the electrochemical cationic process from the anionic process. Following this path demonstrates that the issue of cycle stability clearly can be improved. Optimized $(Li_2Fe)SO$ exhibits a high capacity of around 175 mAh $g^{-1}$, which only marginally decreases by less than 4% over 100 cycles at 1 C if the electrochemical processes are restrained to only the cationic processes. Including the anionic processes yields after a few cycles twice this capacity, but severe fading by more than 75% (typical for Li-rich antiperovskites[3,9,14]) displays that this process is detrimental for cycling stability. Our results further unveil that particle size is not a key parameter for electrochemical performance in Li-rich antiperovskites, but impurities present in the samples govern the observed differences.

## 2. EXPERIMENTAL SECTION

**Synthesis and Structural Characterization.** The synthesis methods employed as well as a detailed physical characterization of the $(Li_2Fe)SO$ samples can be found in ref 13. The $(Li_2Fe)SO$ samples used here have been produced by a ball milling (BM) method. Either pristine material was used or postsynthesis heat treatment at 300 or 500 °C was applied. (The materials under study have been labeled "BM", "300 °C", and "500 °C" in ref 13.) To highlight the synthesis conditions, the samples will henceforth be referred to as BM, BM300, and BM500. X-ray diffraction studies have been performed (STOE STADI P) in Debye−Scherrer mode with a Mo $K\alpha_1$ radiation source ($\lambda = 0.70926$ Å) and a Mythen 1 K detector (Dectris). To prevent any air exposure, the samples were filled into glass capillaries inside an argon glovebox and then melt sealed.

**Magnetic Measurements.** Magnetic measurements were performed on $(Li_2Fe)SO$ powder samples using a MPMS3 magnetometer (Quantum Design). The static magnetic susceptibility $\chi = M/B$ has been obtained upon varying the temperature between 120 and 350 K at 1 T by using field-cooled (FC) and zero-field-cooled (ZFC) protocols where the sample was cooled either in the external measurement field or the field was applied after cooling to the lowest temperature. Isothermal magnetization $M(B)$ has been obtained at $T = 1.8$ K in the field range $-7\ \mathrm{T} \leq B \leq +7\ \mathrm{T}$.

**Electrochemical Measurements.** Electrode and battery assembly was performed in an argon-filled glovebox with controlled humidity and oxygen concentration due to the moisture sensitivity of $(Li_2Fe)SO$. The electrode slurry was prepared by mixing the active material, carbon black, and poly(vinylidene fluoride) with a ratio of 70:15:15 (wt %) in anhydrous isopropanol. Afterward, the resulting mixture was spread onto a (Ø = 10 mm) aluminum mesh current collector to manufacture electrodes with an active material mass loading between 3.2 and 6.3 mg per $cm^{-2}$ (see ref 18). The obtained electrodes were thereafter dried overnight at room temperature and then pressed at around 7.5 MPa. A glass fiber separator (Whatman GF/D) and a pure lithium metal foil counter electrode were used.[19] The electrolyte was composed of 1 M $LiPF_6$ in a mixture of ethylene carbonate and dimethyl carbonate (1:1 by volume, Aldrich). Electrochemical measurements were carried out using a VMP3 potentiostat and a BCS-805 (BioLogic) at 25 °C. Cyclic voltammetry (CV) and galvanostatic cycle measurements with potential limitation (GCPL) were performed in a 2032 coin cell housing.[20] Note, the theoretical capacity of $(Li_2Fe)SO$ for the extraction/insertion of 1 $Li^+$ is 227.57 mAh $g^{-1}$, and the rate 1 C is defined as the charge/discharge current required to extract/insert 1 $Li^+$ from/into the antiperovskite material within 1 h.

## 3. RESULTS AND DISCUSSION

Figure 1 displays powder XRD patterns of the mechanochemically synthesized $(Li_2Fe)SO$-BM, $(Li_2Fe)SO$-BM300, and

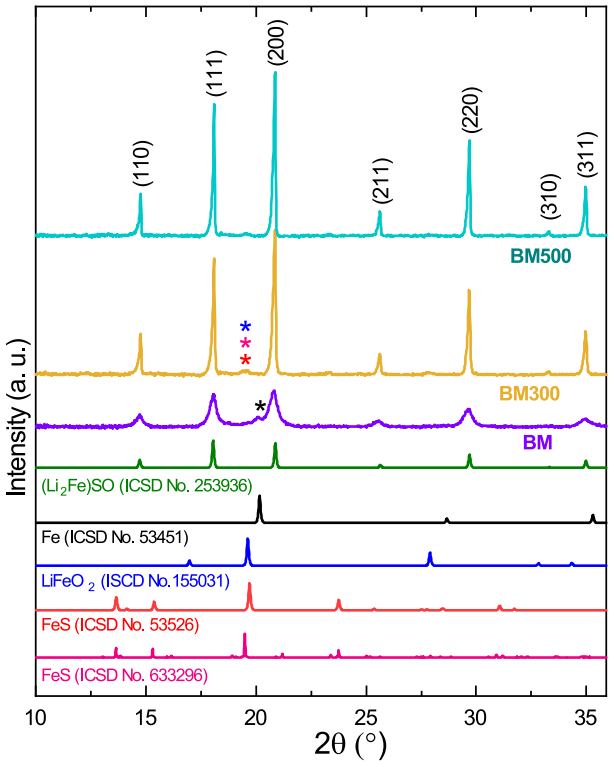


**Figure 1.** XRD patterns of BM, BM300, and BM500 as well as reference patterns for $(Li_2Fe)SO$ (ICSD No. 253936[1]), Fe (ICSD No. 53451[21]), $LiFeO_2$ (ICSD No. 155031[22]), and FeS (ICSD Nos. 53526[23] and 633296[24]). The Miller indices ($hkl$) of the peaks correspond to the $(Li_2Fe)SO$ (ICSD No. 253936[1]) reference. The asterisks (*) mark reflexes between 18° and 20° attributed to tiny impurities. The colors used for the asterisks symbolize distinct phases.

$(Li_2Fe)SO$-BM500 together with the reference patterns of $(Li_2Fe)SO$ (ICSD No. 253936[1]) and some possible impurity phases: Fe (ICSD No. 53451[21]), $LiFeO_2$ (ICSD No. 155031[22]), and FeS (ICSD No. 53526[23] and 633296[24]). The cubic antiperovskite structure with $Pm\bar{3}m$ space group is clearly the main phase for all three materials. Small additional peaks appearing mostly between 19° and 20° in the patterns of the $(Li_2Fe)SO$ samples are associated with the presence of crystalline impurities. We refer to Figure S1 in the Supporting Information for a closer look at the patterns. The data imply that the BM material contains an iron impurity phase. After subsequent heat treatment (BM300, BM500) this phase is however no longer present. All samples show a small elevation around 19.5° which may indicate either FeS and/or $LiFeO_2$. Given the very similar reflexes at around 19.5° of FeS and


https://doi.org/10.1021/acsami.4c05800
ACS Appl. Mater. Interfaces 2024, 16, 40873−40880

$LiFeO_2$, it is not possible to make a conclusive determination based on the XRD data alone.

The fact that many iron-based materials show long-range magnetic order renders measurement of the magnetization a particularly suitable tool to determine and quantify potential foreign phases with exceptionally high sensitivity.[25] Figure 2a

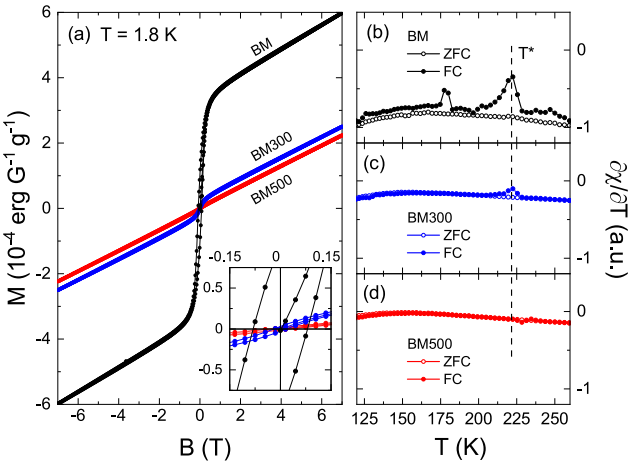


**Figure 2.** (a) Isothermal magnetization of BM, BM300, and BM500 vs magnetic field at 1.8 K. Temperature derivative of the static magnetic susceptibility ($\chi = M/B$) of the BM (b), BM300 (c), and BM500 (d) sample vs temperature at $B$ = 1 T in the temperature range between 120 and 260 K. Both FC (orange) and ZFC (gray) protocols have been applied. The anomaly labeled by $T^*$ signals a tiny $Fe_{0.95}S$ impurity phase, which strongly decreases for BM300 and vanishes for BM500.

depicts the isothermal field-dependent magnetization $M(B)$ at 1.8 K for all three materials under study. While in all three materials the magnetic susceptibility $\partial M/\partial B(|B| \gtrsim 1\ \mathrm{T})$ is very similar, there is a pronounced difference around zero field. Specifically, there is a large jump in magnetization for BM which is strongly reduced in BM300 and nearly vanishes for BM500. The data imply ferromagnetic moments of $M_s$ = 3.3(1), 0.23(1), and 0.05(5) erg $G^{-1}$ $g^{-1}$ for BM, BM300, and BM500, respectively. Hence, while BM shows a well-visible ferromagnetic impurity phase, it decreases by 1 and 2 orders of magnitude upon heat treatment at 300 and 500 °C, respectively. By attributing the ferromagnetic signal to an iron impurity phase, comparison of $M_s$ with the saturation magnetization of iron $M_s^{Fe}$ = 220.25 erg $G^{-1}$ $g^{-1}$ (see ref 26) yields a contained iron impurity with a maximum of 1.4 wt %. This value agrees well with 1.2 vol % for BM inferred from XRD data.[13] We note, however, that $M_s$ can contain contributions of other ferro- or ferrimagnetic impurity phases like $Fe_{1-x}S_x$ or $LiFeO_2$, which cannot be ruled out either.

The temperature dependence of the temperature derivative $\partial\chi/\partial T$ of the pristine material BM (Figure 2b) confirms the presence of an additional impurity phase. Specifically, the FC data displays an anomaly at $T^* \simeq 222$ K, indicative for an antiferromagnetic transition which we attribute to the alpha transition in $Fe_{0.95}S$.[27] The associated anomaly at $T^*$ strongly decreases for BM300 and vanishes for BM500 (see Figure 2b–d). The anomaly observed at 178 K in the BM sample can be attributed to the iron–sulfur compound $Fe_{0.9375}S$.[27] In the BM300 sample, this anomaly and thus $Fe_{0.937}S$ has vanished completely.

Cyclic voltammetry is used to investigate the electrochemical processes in BM, BM300, and BM500 in detail. Notably, the cyclic voltammograms (CVs) of all three $(Li_2Fe)SO$ materials in Figure 3 demonstrate a comparable

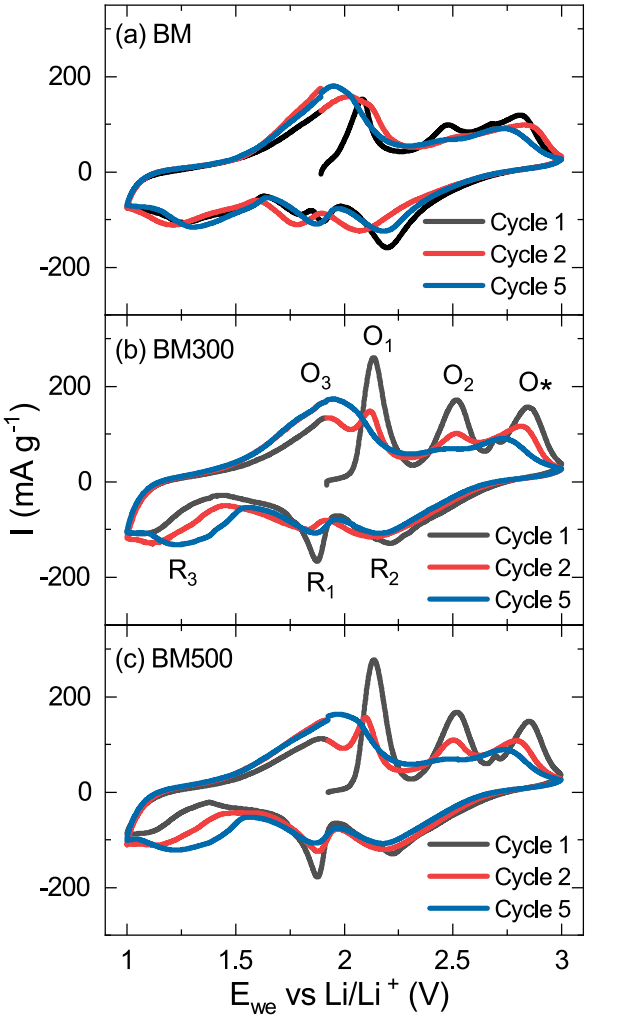


**Figure 3.** Cyclic voltammograms of cycles 1, 2, and 5 of (a) BM, (b) BM300, and (c) BM500 measured at a scan rate of 0.1 mV $s^{-1}$. The labels R/O mark distinct reduction and oxidation features.

multistage lithium extraction and insertion mechanism. Independent on the synthesis conditions, the two initial oxidation peaks $O_1$ and $O_2$ appear at about 2.1 and 2.5 V and signal the two-stage cationic $Fe^{2+}$ to $Fe^{3+}$ oxidation process.[3] The high-voltage oxidation peak O* at 2.8 V is believed to be originating from an anionic reaction.[3] During the first intercalation (discharge), all three samples display distinct reduction peaks ($R_1$, $R_2$, and $R_3$). This observation is consistent with previous research on solid-state reaction (SSR) synthesized $(Li_2Fe)SO$.[3,10] The insertion and removal of lithium via multiple stages moreover is observed in all lithium-rich antiperovskites investigated so far and can therefore be assumed to be a general feature of this material class. The same is true for the decrease of the initial differences in the electrochemical properties of the different materials after only a few cycles. Based on our previous work on $(Li_2Fe)SeO$,[14] where we showed that the high-voltage anionic processes are crucial for the electrochemical performance and properties, CV measurements were performed for the three


https://doi.org/10.1021/acsami.4c05800
ACS Appl. Mater. Interfaces 2024, 16, 40873–40880

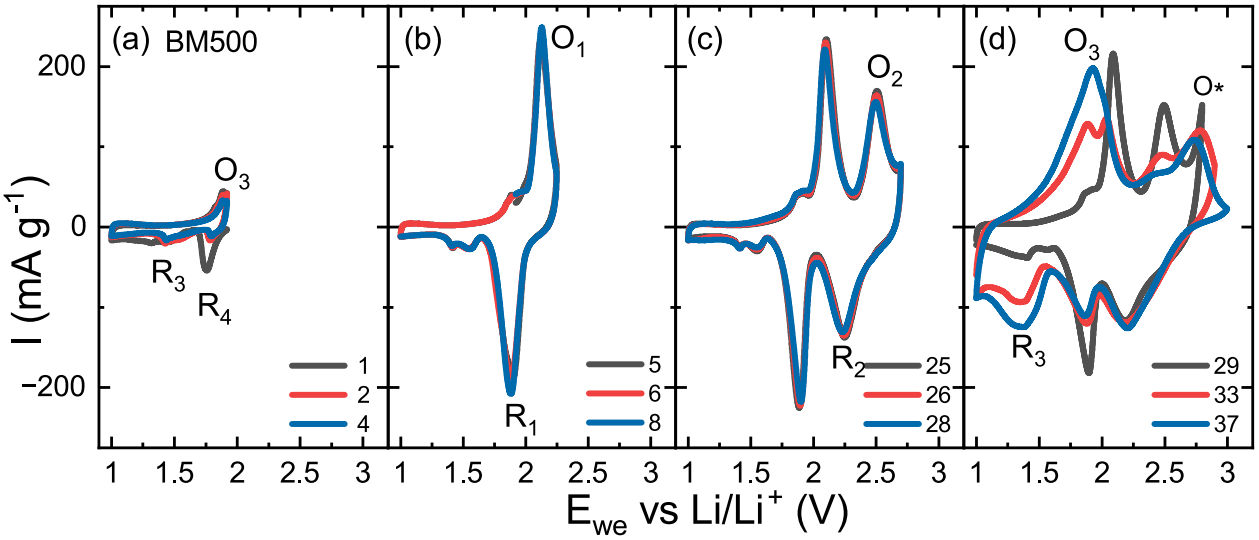


**Figure 4.** Cyclic voltammograms of BM500 in the potential range from 1 V to (a) OCV, (b) 2.3, and (c) 2.7 V to (d) 2.8 V (cycle 29), 2.9 (cycle 33), and 3 V (cycle 37) vs $Li/Li^+$ measured at a scan rate of 0.1 mV $s^{-1}$. The labels R/O correspond to those in Figure 3.

$(Li_2Fe)SO$ materials under study where the maximum voltage is stepwise increased (see Figure 4 for BM500 and Figure S2 in the Supporting Information for BM and BM300). The measurements shown here were carried out on a single cell, whereby the maximum voltage was increased by a 0.1 V step after an interval of 4 cycles in one voltage range. Here, a special focus was placed on the separation of cationic and anionic redox activity.

CV measurements with initial lithiation (discharge) to 1 V and the restriction of the maximum voltage to OCV (Figure 4a and Figure S2) show the electrochemical behavior at initial intercalation. Restricting the voltage only to the regime of lithium insertion provides the possibility to study the electrochemical activity of possible lithium vacancies or active anodic impurity phases. The data in Figure 4a and Figure S2a–c reveal electrochemical activity signaled by $R_3$ at approximately 1.4 V and $O_3$ at 2 V, which originates from the following conversion reaction of $Fe_{1-x}S_x$[28−31]

$$FeS + 2Li^+ + 2e^- \leftrightarrow Li_2S + Fe \quad (1)$$

Iron-based sulfates are due to their high-capacity potential battery material in many different cell chemistries.[32−35] The comparison between the three different materials displays that the electrochemical fingerprints of $Fe_{1-x}S_x$ strongly decrease in the postsynthesis heat-treated materials as evidenced by the decrease of the $R_3/O_3$ redox peaks. This is in accordance with our magnetization data, which also show the strong decrease of the contained $Fe_{0.95}S$ phase in the heat-treated materials BM300/BM500. The additional peak at approximately 1.8 V, labeled as R4, can be attributed to an iron sulfide phase with a slightly altered stoichiometry compared to the one responsible for R3/O3. The sharp decrease of R4 after the first cycle is most likely due to the fact that the corresponding oxidation reaction lies partly outside the selected potential window. This hypothesis is supported by the increase in the maximum measured current at R4 from 8 to 28 mA $g^{-1}$ when the maximum voltage is increased from OCV to 2.3 V. Additionally, during direct charging (Figure 3c), no electrochemical activity is observed before the initial iron oxidation (O1). However, if lithium is inserted directly (see Figure 4a–c), two small peaks are visible before the iron oxidation. This observation again supports the hypothesis of electrochemically active tiny iron−sulfur phases present in our material.

Complementary GCPL measurements provide further insights into the extent of charge conversion (see Figure S3a–c). The data reveal a substantial conversion of charges of the contained impurity phases of approximately 100 mAh $g^{-1}$ for BM, around 45 mAh $g^{-1}$ for BM300, and 20 mAh $g^{-1}$ for BM500. An estimate based on the fraction of $Fe_{1-x}S_x$ in the BM sample by comparing the converted capacity at $R_3$ of approximately 70 mAh $g^{-1}$ with the theoretical capacity of FeS (609 mAh $g^{-1}$)[31] and $FeS_2$ (894 mAh $g^{-1}$)[31] leads to a possible content between 11% and 7% of $Fe_{1-x}S_x$ in the pristine BM material. For BM300, the capacity associated with $R_3$ is around 30 mAh $g^{-1}$, which leads to an estimated content between 5% and 3% and for BM500 with only around 20 mAh $g^{-1}$ to a content between 3% and 2%. Note that this calculation tends to underestimate as conversion of the full theoretical capacity is rather unlikely.

Increasing the upper potential limit (see Figure 4b and 4c) allows us to comprehensively study the stepwise redox dynamics involving the $Fe^{2+} \leftrightarrow Fe^{3+}$ pair. By increasing the voltage up to 2.7 V, two redox pairs O1/R1 (see Figure 4b) and O2/R2 (see Figure 4c) occur successively, which can be attributed to the two-stage (O1, R1 first part and O2, R2 s part) $Fe^{2+}/Fe^{3+}$ redox process of the antiperovskite phase.[3] In consecutive cycles, the CV curves nearly perfectly overlap, which implies highly reversible and stable processes. For Figure 4b–d, it is possible to make statements about the stability of individual processes despite previously performed cycles, as the CV curves overlap considerably and only minimal and insignificant changes occur.

When extending the CVs to the full potential range of 1−3 V and thereby including the high-voltage anionic process $O_*$ as shown in Figure 4d, all samples show a significant change of the CV curves with a pronounced nonreversible element. Specifically, the pair $R_3/O_3$ in the low-voltage range which is attributed to the electrochemical activity of $Fe_{1-x}S_x$ increases drastically, while simultaneously, a significant decrease in the antiperovskite-associated oxidation processes ($O_1$, $O_2$, and $O_*$) is observed. Both the appearance of an extra feature as well as observed irreversibility is similar to what is found in


https://doi.org/10.1021/acsami.4c05800
ACS Appl. Mater. Interfaces 2024, 16, 40873−40880

$(Li_2Fe)SeO$.[14] We therefore conclude that during the anionic O* process, the antiperovskite phase decomposed and one or several iron sulfide phases are formed.

To determine the cutoff voltage at which the irreversible oxidation reaction $O_*$ set in, GCPL measurements using a constant current constant voltage protocol and a step-like increase of the maximum voltage in 0.1 V increments was performed (see Figure S3d–f). For all $(Li_2Fe)SO$ materials under study, the threshold voltage beyond which the antiperovskite material deteriorates and $Fe_{1-x}S_x$ is produced amounts to 2.7 V, i.e., it is not affected by the above-discussed material changes due to heat treatment. As seen in the data, for all three materials we find an increase in the low-voltage reactions as soon as the maximum voltage exceeds 2.6 V. The stable regime for electrochemical cycling is therefore restricted to a maximum voltage of 2.6 V.

Performance characteristics of BM, BM300, and BM500 are presented in Figure 5a. To evaluate the impact of the high-voltage anionic process on the high-current capability and stability, two sets of measurements were performed: one extending up to 3 V and another one within the limited potential range up to 2.6 V to avoid the anionic process $O_*$. Within the first cycles, two significant trends emerge. First, when cycling up to 3 V, all studied materials exhibit an impressive initial capacity of approximately 400 mAh $g^{-1}$ at a C/10 current rate. This marks a notable achievement and unequivocally underscores the substantial advantages and potential offered by both the material and the chosen synthesis approach. Compared to the initial capacity achieved by previous measurements on lithium-rich antiperovskite cathodes of 285 mAh $g^{-1}$ for $(Li_2Fe)SO$ by Mikhailova et al.,[3] 220 mAh $g^{-1}$ for $(Li_2Fe_{0.8}Mn_{0.2})SO$ by Deng et al.,[12] 245 mAh $g^{-1}$ for $(Li_2Fe)S_{0.7}Se_{0.3}O$ by Mohamed et al.,[16] and 164 and 300 mAh $g^{-1}$ for $(Li_2Fe)SeO$ by Mohamed et al.[17] and Singer et al.,[14] this is by far the highest capacity ever achieved. In contrast, in the constrained potential range, BM, BM300, and BM500 all show capacities around 220 mAh $g^{-1}$. Second, the cycling dependence of all materials is rather similar in the restricted voltage regime but strongly differs in the extended regime. To be specific, when cycling up to 3 V, in the first nine cycles, BM shows a significant loss of capacity, while BM300 and BM500 show an initial increase followed by a significant decrease (see Figure 5a). At higher currents, the differences between the different voltage ranges become even more pronounced: In the full range, we observe average capacities of 261, 188, and 132 mAh $g^{-1}$ at C/4, C/2, and 1 C and 230, 210, 180 mAh $g^{-1}$ in the limited range for BM. For B300, the same measurements yield 325, 240, and 175 mAh $g^{-1}$ (full range) and 220, 210, 187 mAh $g^{-1}$ (limited range) and for BM500 250, 150, and 95 mAh $g^{-1}$ (full range) and 205, 200, 172 mAh $g^{-1}$ (limited range). Overall, the limited potential range is clearly beneficial for all materials. First and foremost, it results in drastically improved cycling stability as well as in higher converted capacity at high currents. We also particularly emphasize the very good high-current capability of the $(Li_2Fe)SO$ samples in the limited range, which only show low reductions of around 20% in capacity with a 10-fold increase in current.

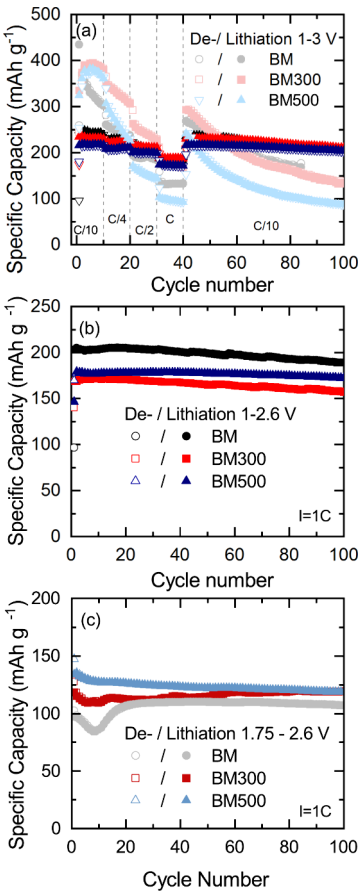


**Figure 5.** (a) Rate performance of $(Li_2Fe)SO$-BM, -BM300, and -BM500 in the potential window 1–3 and 1–2.6 V. Specific discharge/charge capacities of BM, -BM300, and -BM500 in the potential window (b) from 1 to 2.6 V and (c) between 1.75 and 2.6 V at 1 C. Note that the legend in b also describes data with the matching color in a.

The outstanding electrochemical capabilities and stability achieved for $(Li_2Fe)SeO$ when avoiding the high-voltage anionic reaction are validated by galvanostatic cycling experiments conducted at a rate of 1 C as presented in Figure 5b. Specifically, the initial capacity reaches approximately 200 mAh $g^{-1}$ in the case of BM, 175 mAh $g^{-1}$ for BM500, and 170 mAh $g^{-1}$ for BM300. The best cycling stability of the materials under study is found for BM500, which shows 96% capacity retention after 100 cycles. Note that this is indeed the highest capacity retention ever reported for a lithium-rich antiperovskite material.

In order to quantify and separate the contributions of impurity phases to the observed reversible capacity, further studies with the minimum voltage limited to 1.75 V are shown in Figure 5c. In this potential range, we expect no electrochemical activity from impurity phases (active only below 1.75 V (see Figure S3)), so that the resulting capacity can be completely attributed to the $(Li_2Fe)SO$ component.

Figure 5c shows that the capacity of the BM material is reduced by 100 mAh $g^{-1}$ when cycling in the regime 1.75–2.6 V. This difference corresponds very well to the value obtained by direct discharge (see Figure S3a) which hence further evidences that impurity phases are electrochemically not active above 1.75 V. Note that the actual capacity arising from the antiperovskite phase is higher than that given in Figure 5c as the specific capacity is normalized to the total mass which, depending on the postsynthesis treatment, includes amounts of in this voltage window inactive impurity phases. The fact that the BM sample contains the highest proportion of now inactive


https://doi.org/10.1021/acsami.4c05800
ACS Appl. Mater. Interfaces 2024, 16, 40873–40880

foreign phase among the studied materials hence straightforwardly explains that its capacity in Figure 5c is lower than that of BM300 and BM500. In addition to this mass effect, our GCPL and CV studies in Figures S3 and S2 indicate slight but visible differences in kinetics between the samples so that the exact voltages of the relevant processes slightly differ too. This also leads to small differences between the measured capacities of the samples.

The obtained capacities associated with the bare title compounds presented in Figure 5c show substantial changes to the overall capacity data in Figure 5b. First, BM does not show the best performance anymore. After 100 cycles, BM shows a capacity of 110 mAh $g^{-1}$ while BM300 and BM500 present more than 120 mAh $g^{-1}$. In addition, there is a minimum in reversible capacity after a few (~10) cycles. We attribute this behavior to an activation process triggered by changing kinetics (see Figure S4 in the Supporting Information, where an initial decrease followed by an increase of the low-voltage plateau is visible), which is an often seen phenomenon for conversion-based materials.[36−40] We note that for the BM sample a clear separation of the electrochemical activity associated with impurities is not possible due to the broader voltage window at which they are occurring and the resulting high overlap of the electrochemical activity of the iron sulfide impurity and the antiperovskite phase (see Figures S2 and S3). The BM sample therefore still displays a small fraction of the electrochemical activity of the contained iron sulfide.

In general, Figure 5c clearly shows that in the first 100 cycles the electrochemical performance of the bare antiperovskite phase is almost independent of the post-treatment method. The fact that the particle sizes of the materials strongly differ (submicrometer- to few micrometer-sized particles (BM) compared to particles above the 10 $\mu$m range (BM500)[13]) indicates the high ionic conductivity of the $(Li_2Fe)SO$ phase and highlights its potential for lithium-ion battery application.

Long-term galvanostatic cycling studies of BM, BM300, and BM500 in the restricted potential range from 1 to 2.6 V and from 1.75 to 2.6 V together with the Coulombic efficiency shown in Figure S5 in the SI give further insights into the practically accessible capacity. In the range from 1 to 2.6 V, BM, BM300, and BM500 show drops of 32%, 38%, and 29% over 400 cycles. Here, we note the artificially high Coulombic efficiency (CE) of the BM sample of around 200% in the first cycle. This high CE is only possible due to the lithium metal counter electrode, while in a full-cell experiment, the maximum achievable value in the following cycles is restricted to the discharge capacity of approximately 100 mAh $g^{-1}$. Further restriction to only the antiperovskite processes (voltage range from 1.75 to 2.6 V, Figure S4b) leads to a discernible reduction in the Coulombic efficiency (CE) to approximately 95%. Restricting the voltage window to 1.75−2.6 V therefore effectively minimizes the loss of practically achievable capacity to around 5% after the first cycle, compared to a 50% loss with the low-voltage limit of 1 V (see Figure S5a). At the same time, an improvement in cycle stability can be observed, as shown by the BM300 example, which has a loss of only 5% in over 400 cycles compared to 38% in the extended voltage range 1−2.6 V. These results imply two major findings. (1) The cationic electrochemical processes of $(Li_2Fe)SO$ are overall very stable. (2) Further performance improvements can be obtained by reducing the amount of impurities and prevention of the conversion reaction $O_*$.

## 4. CONCLUSIONS

Our detailed electrochemical study on lithium-rich antiperovskite cathode materials allows us to separate cationic and anionic redox processes. With the high-voltage anionic process, an astonishing electrochemical capacity of around 400 mAh $g^{-1}$ is initially reachable. Our results however also demonstrate that the high-voltage anionic process is the root cause of the poor cycling stability reported in all previous studies on lithium-rich antiperovskites. By avoiding the so-called anionic process ($O_*$), a highly improved cycling stability is achieved. The success of this approach is proven with the BM500 sample, which exhibits at 1 C only 4% capacity fading over 100 cycles at the remarkable capacity of about 175 mAh $g^{-1}$. The data hence prove drastic performance improvements of $(Li_2Fe)SO$. While strongly differing particle sizes do not visibly affect the electrochemical performance of the materials under study, impurities are a key factor. In addition, by appropriately restricting the voltage regime we have also investigated the electrochemical performance of the bare antiperovskite phase, which in the restricted voltage regime provides over 400 cycles a stable capacity of about 110 mAh $g^{-1}$. In summary, by separating cationic and anionic redox activity we have shown the consequences of each process as well as the implications on the overall electrochemical performance. Our data highlight the potential of the pure cationic electrochemical reaction in lithium-rich antiperovskites, thereby showing the route to further improve their performance in electrochemical energy storage.

## ■ ASSOCIATED CONTENT

### Supporting Information

The Supporting Information is available free of charge at https://pubs.acs.org/doi/10.1021/acsami.4c05800.

X-ray diffractograms of all samples in higher magnification; selected cyclic voltammograms of all samples, where the maximum voltage was stepwise increased, in order to highlight the stability and effect of the individual processes; GCPL measurement of the cutoff voltage; selected potential lines, corresponding to Figure 5; long-term GCPL + Coulombic efficiencies of all samples at 1 C in the restricted range from 1 to 2.6 V and from 1.75 to 2.6 V (PDF)

## ■ AUTHOR INFORMATION


### Corresponding Authors

**Lennart Singer** − *Kirchhoff Institute for Physics, Heidelberg University, 69120 Heidelberg, Germany;* orcid.org/0000-0002-4882-9729; Email: lennart.singer@kip.uni-heidelberg.de

**Rüdiger Klingeler** − *Kirchhoff Institute for Physics, Heidelberg University, 69120 Heidelberg, Germany*; Email: klingeler@kip.uni-heidelberg.de

### Authors

**Bowen Dong** − *Kirchhoff Institute for Physics, Heidelberg University, 69120 Heidelberg, Germany*

**Mohamed A. A. Mohamed** − *Leibniz Institute for Solid State and Materials Research (IFW) Dresden, 01069 Dresden, Germany; Department of Physics, Faculty of Science, Sohag University, 82524 Sohag, Egypt*

**Frederik L. Carstens** − *Kirchhoff Institute for Physics, Heidelberg University, 69120 Heidelberg, Germany*

**Silke Hampel** − *Leibniz Institute for Solid State and Materials Research (IFW) Dresden, 01069 Dresden, Germany*
**Nico Gräßler** − *Leibniz Institute for Solid State and Materials Research (IFW) Dresden, 01069 Dresden, Germany;* orcid.org/0000-0002-3437-3724

Complete contact information is available at: https://pubs.acs.org/10.1021/acsami.4c05800

### Author Contributions

Conceptualization: L.S. and R.K. Synthesis and materials characterization: M.M., S.H., and N.G. Electrochemical studies: L.S. and B.D. Magnetic studies: L.S. and F.L.C. Writing—original draft preparation: L.S. and R.K. Writing—review and editing: L.S. and R.K. Visualization: L.S. Supervision: R.K. All authors have read and agreed to the published version of the manuscript.

### Notes

The authors declare no competing financial interest.

## ■ ACKNOWLEDGMENTS

Financial support by Deutsche Forschungsgemeinschaft (DFG) through projects KL 1824/20-1 and GR 5987/2-1 is acknowledged. Work was also supported within the framework of the Excellence Strategy of the Federal and State Governments of Germany via Heidelberg University's flagship EMS initiative. M.A.A.M. thanks the IFW excellence program for financial support.

## ■ REFERENCES

(1) Lai, K. T.; Antonyshyn, I.; Prots, Y.; Valldor, M. Anti-Perovskite Li-Battery Cathode Materials. *J. Am. Chem. Soc.* **2017**, *139*, 9645−9649.
(2) Assat, G.; Tarascon, J.-M. Fundamental Understanding and Practical Challenges of Anionic Redox Activity in Li-ion Batteries. *Nature Energy* **2018**, *3*, 373−386.
(3) Mikhailova, D.; Giebeler, L.; Maletti, S.; Oswald, S.; Sarapulova, A.; Indris, S.; Hu, Z.; Bednarcik, J.; Valldor, M. Operando Studies of Antiperovskite Lithium Battery Cathode Material $(Li_2Fe)SO$. *ACS Appl. Energy Mater.* **2018**, *1*, 6593−6599.
(4) Lu, Z.; Ciucci, F. Anti-perovskite Cathodes for Lithium Batteries. *Journal of Materials Chemistry A* **2018**, *6*, 5185−5192.
(5) Song, H.; Luo, M.; Wang, A. High Rate and Stable Li-Ion Insertion in Oxygen-Deficient $LiV_3O_8$ Nanosheets as a Cathode Material for Lithium-Ion Battery. *ACS Appl. Mater. Interfaces* **2017**, *9*, 2875−2882.
(6) Cui, S.-L.; Xiao, Z.-X.; Cui, B.-C.; Liu, S.; Gao, X.-P.; Li, G.-R. Fast Charge-Transport Interface on Primary Particles Boosts High-Rate Performance of Li-Rich Mn-Based Cathode Materials. *ACS Appl. Mater. Interfaces* **2023**, *15*, 13195−13204.
(7) Deng, Z.; Ni, D.; Chen, D.; Bian, Y.; Li, S.; Wang, Z.; Zhao, Y. Anti-perovskite Materials for Energy Storage Batteries. *InfoMat* **2022**, *4*, 476.
(8) Dai, T.; Kouoi, X.; Reynaud, M.; Wagemaker, M.; Valldor, M.; Famprikis, T.; Koposov, A. Y. Antiperovskite Active Materials for Metal-ion Batteries: Expected Advantages, Limitations, and Perspectives. *Energy Storage Materials* **2024**, *68*, 103363.
(9) Gorbunov, M. V.; Carrocci, S.; Maletti, S.; Valldor, M.; Doert, T.; Hampel, S.; Gonzalez Martinez, I. G.; Mikhailova, D.; Gräßler, N. Synthesis of $(Li_2Fe_{1-y}Mn_y)SO$ Antiperovskites with Comprehensive Investigations of $(Li_2Fe_{0.5}Mn_{0.5})SO$ as Cathode in Li-ion Batteries. *Inorg. Chem.* **2020**, *59*, 15626−15635.
(10) Gorbunov, M. V.; Carocci, S.; Gonzalez Martinez, I. G.; Baran, V.; Mikhailova, D. Studies of $Li_2Fe_{0.9}M_{0.1}SO$ Antiperovskite Materials for Lithium−Ion Batteries: The Role of Partial $Fe^{2+}$ to $M^{2+}$ Substitution. *Front. Energy Res.* **2021**, *9*, 360.
(11) Miura, M.; Hikima, K.; Matsuda, A. Fabrication and Electrochemical Characterization of an All-solid-state Battery with an Anti-perovskite Electrode Material $(Li_2Fe)SO$. *Chem. Lett.* **2022**, *51*, 690−692.
(12) Deng, Z.; Chen, D.; Ou, M.; Zhang, Y.; Xu, J.; Ni, D.; Ji, Z.; Han, J.; Sun, Y.; Li, S.; Ouyang, C.; Wang, Z. Cation Disordered Anti−Perovskite Cathode Materials with Enhanced Lithium Diffusion and Suppressed Phase Transition. *Adv. Energy Mater.* **2023**, *13*, 2300695.
(13) Mohamed, M. A. A.; Saadallah, H. A. A.; Gonzalez-Martinez, I. G.; Hantusch, M.; Valldor, M.; Büchner, B.; Hampel, S.; Gräßler, N. Mechanochemical Synthesis of Li-rich $(Li_2Fe)SO$ Cathode for Li-ion Batteries. *Green Chem.* **2023**, *25*, 3878−3887.
(14) Singer, L.; Mohamed, M. A. A.; Hahn, H.; Gonzalez-Martinez, I. G.; Hantusch, M.; Wenelska, K.; Mijowska, E.; Büchner, B.; Hampel, S.; Gräßler, N.; Klingeler, R. Elucidating the Electrochemical Reaction Mechanism of Lithium-rich Antiperovskite Cathodes for Lithium-ion Batteries as Exemplified by $(Li_2Fe)SeO$. *J. Mater. Chem. A* **2023**, *11*, 14294−14303.
(15) Lai, K. T.; Antonyshyn, I.; Prots, Y.; Valldor, M. Extended Chemical Flexibility of Cubic Anti-Perovskite Lithium Battery Cathode Materials. *Inorg. Chem.* **2018**, *57*, 13296−13299.
(16) Mohamed, M. A. A.; Gorbunov, M. V.; Valldor, M.; Hampel, S.; Gräßler, N.; Mikhailova, D. Tuning the Electrochemical Properties by Anionic Substitution of Li-rich Antiperovskite $(Li_2Fe)S_{1-x}Se_xO$ Cathodes for Li-ion Batteries. *J. Mater. Chem. A* **2021**, *9*, 23095−23105.
(17) Mohamed, M.A.A.; Singer, L.; Hahn, H.; Djendjur, D.; Ozkara, A.; Thauer, E.; Gonzalez-Martinez, I.G.; Hantusch, M.; Büchner, B.; Hampel, S.; Klingeler, R.; Gräßler, N. Lithium-rich Antiperovskite $(Li_2Fe)SeO$: A High-performance Cathode Material for Lithium-ion Batteries. *J. Power Sources* **2023**, *558*, 232547.
(18) Ottmann, A.; Zakharova, G. S.; Ehrstein, B.; Klingeler, R. Electrochemical Performance of Single Crystal Belt-like $NH_4V_3O_8$ as Cathode Material for Lithium-ion Batteries. *Electrochim. Acta* **2015**, *174*, 682−687.
(19) Singer, L.; Kukułka, W.; Thauer, E.; Gräßler, N.; Asyuda, A.; Zharnikov, M.; Mijowska, E.; Klingeler, R. On the Rising Extra Storage Capacity of Ultra-small $Fe_3O_4$ Particles Functionalized with HCS and their Potential as High-performance Anode Material for Electrochemical Energy Storage. *Electrochim. Acta* **2023**, *448*, 142155.
(20) Zakharova, G. S.; Singer, L.; Fattakhova, Z. A.; Wegener, S.; Thauer, E.; Zhu, Q.; Shalaeva, E. V.; Klingeler, R. $MoO_2$/C Composites Prepared by Tartaric Acid and Glucose-assisted Sol-gel Processes as Anode Materials for Lithium-ion Batteries. *J. Alloys Compd.* **2021**, *863*, 158353.
(21) Kohlhaas, R.; Dunner, P.; Schmitz-Pranghe, N. Über die Temperaturabhängigkeit der Gitterparameter von Eisen Kobalt und Nickel im Bereich hoher Temperaturen. *Z. Angew. Phys.* **1967**, *23*, 245−249.
(22) Vucinic-Vasic, M.; Antic, B.; Blanusa, J.; Rakic, S.; Kremenović, A.; Nikolic, A. S.; Kapor, A. Formation of Nanosize Li-ferrites from Acetylacetonato Complexes and their Crystal Structure, Microstructure and Order−disorder Phase Transition. *Appl. Phys. A: Mater. Sci. Process.* **2006**, *82*, 49−54.
(23) Coey, J.; Roux-Buisson, H. Electronic Properties of $(Ni_{1-x}Fe_x)s$ Solid Solutions. *Mater. Res. Bull.* **1979**, *14*, 711−716.
(24) Morimoto, N.; Nakazawa, H.; Nishigucmi, K.; Tokonami, M. Pyrrhotites: Stoichiometric Compounds with Composition $Fe_{n-1}S_n$ ($n \geq 8$). *Science (New York, N.Y.)* **1970**, *168*, 964−966.
(25) Chernova, N. A.; Nolis, G. M.; Omenya, F. O.; Zhou, H.; Li, Z.; Whittingham, M. S. What Can We Learn About Battery Materials From their Magnetic Properties? *J. Mater. Chem.* **2011**, *21*, 9865−9875.
(26) Bozorth, R. M. *Ferromagnetism*; IEEE Press John Wiley& Sons Inc., and IEEE Xplore, 1978.
(27) Adachi, K.; Ogawa, S. *Landolt-Börnstein Zahlenwerte und Funktionen aus Naturwissenschaften und Technik: Neue Serie* =

*Numerical Data and Functional Relationships in Science and Technology: New Series*; Springer: Berlin, 1988; Vol. *27A*.
(28) Fei, L.; Lin, Q.; Yuan, B.; Chen, G.; Xie, P.; Li, Y.; Xu, Y.; Deng, S.; Smirnov, S.; Luo, H. Reduced Graphene Oxide Wrapped FeS Nanocomposite for Lithium-ion Battery Anode with Improved Performance. *ACS Appl. Mater. Interfaces* **2013**, *5*, 5330−5335.
(29) Liu, X.; Wu, Y.; Li, X.; Yu, J.; Sun, Y. FeS@onion-like Carbon Nanocapsules Embedded in Amorphous Carbon for the Lithium Ion Batteries with Excellent Cycling Stability. *Ceram. Int.* **2018**, *44*, 13654−13661.
(30) Cao, Z.; Ma, X.; Dong, W.; Wang, H. FeS@tubular Mesoporous Carbon as High Capacity and Long Cycle Life Anode Materials for Lithium- and Sodium-ions Batteries. *J. Alloys Compd.* **2019**, *786*, 523−529.
(31) Xu, Q.-T.; Li, J.-C.; Xue, H.-G.; Guo, S.-P. Binary Iron Sulfides as Anode Materials for Rechargeable Batteries: Crystal Structures, Syntheses, and Electrochemical Performance. *J. Power Sources* **2018**, *379*, 41−52.
(32) Liao, J.; Hu, Q.; Du, Y.; Li, J.; Duan, L.; Bao, J.; Zhou, X. Robust Carbon Nanotube-interwoven $KFeSO_4F$ Microspheres as Reliable Potassium Cathodes. *Science Bulletin* **2022**, *67*, 2208−2215.
(33) Du, Y.; Weng, W.; Zhang, Z.; He, Y.; Xu, J.; Sun, J.; Liao, J.; Bao, J.; Zhou, X. Candied-Haws-like Architecture Consisting of $FeS_2$@C Core-Shell Particles for Efficient Potassium Storage. *ACS Materials Lett.* **2021**, *3*, 356−363.
(34) Song, L.; Zhang, S.; Duan, L.; Li, R.; Xu, Y.; Liao, J.; Sun, L.; Zhou, X.; Guo, Z. Tunable Interfacial Electric Field-Mediated Cobalt-Doped $FeSe/Fe_3Se_4$ Heterostructure for High-Efficiency Potassium Storage. *Angew. Chem., Int. Ed.* **2024**, *63*, e202405648.
(35) Qu, Z.; Zhang, X.; Xiao, R.; Sun, Z.; Li, F. Application of Organosulfur Compounds in Lithium-Sulfur Batteries. *Acta Physico Chimica Sinica* **2023**, *0*, 2301019.
(36) Guo, J.; Liu, Q.; Wang, C.; Zachariah, M. R. Interdispersed Amorphous $MnO_x$-Carbon Nanocomposites with Superior Electrochemical Performance as Lithium-Storage Material. *Adv. Funct. Mater.* **2012**, *22*, 803−811.
(37) Yu, S.-H.; Lee, S. H.; Lee, D. J.; Sung, Y.-E.; Hyeon, T. Conversion Reaction-Based Oxide Nanomaterials for Lithium Ion Battery Anodes. *Small* **2016**, *12*, 2146−2172.
(38) Zou, F.; Chen, Y.-M.; Liu, K.; Yu, Z.; Liang, W.; Bhaway, S. M.; Gao, M.; Zhu, Y. Metal Organic Frameworks Derived Hierarchical Hollow NiO/Ni/Graphene Composites for Lithium and Sodium Storage. *ACS Nano* **2016**, *10*, 377−386.
(39) Sun, X.; Si, W.; Liu, X.; Deng, J.; Xi, L.; Liu, L.; Yan, C.; Schmidt, O. G. Multifunctional Ni/NiO Hybrid Nanomembranes as Anode Materials for High-rate Li-ion Batteries. *Nano Energy* **2014**, *9*, 168−175.
(40) Wang, X.; Wang, J.; Chen, Z.; Yang, K.; Zhang, Z.; Shi, Z.; Mei, T.; Qian, J.; Li, J.; Wang, X. Yolk-double Shell $Fe_3O_4$@C@C Composite as High-performance Anode Materials for Lithium-ion Batteries. *J. Alloys Compd.* **2020**, *822*, 153656.


https://doi.org/10.1021/acsami.4c05800
*ACS Appl. Mater. Interfaces* 2024, 16, 40873−40880